Tarquini *et al. Int J Concr Struct Mater* (2020) 14:2
https://doi.org/10.1186/s40069-019-0381-9

International Journal of Concrete Structures and Materials

RESEARCH Open Access

Extended Tension Chord Model for Boundary Elements of RC Walls Accounting for Anchorage Slip and Lap Splices Presence

Danilo Tarquini[1], João Pacheco de Almeida[2*] and Katrin Beyer[1]

Abstract

This paper presents a mechanical model for the simulation of reinforced concrete (RC) wall boundary elements with lap splices, which builds on the tension chord model. The model is composed of an assembly of components, each one accounting for a different source of deformation. Namely: (i) an anchorage-slip element accounting for the strain penetration of the longitudinal reinforcement into the foundation; (ii) a basic tension chord element evaluating the response outside the lap splice zone; and (iii) a lap splice element describing the behaviour within the lap splice region. For an imposed global displacement, the model provides the steel and concrete stress and strain distributions, the crack distribution and opening, as well as the global resisting axial force. For spliced members, the ultimate displacement is computed through a semi-empirical relationship providing the average lap splice strain at failure. Validation is carried out against a series of uniaxial cyclic tests on RC wall boundary elements featuring both continuous and spliced reinforcement; different lap splice lengths and confining reinforcement are considered. Overall, a good match is obtained between numerical and experimental results in terms of crack width, rebar strain distribution along the splices and ultimate displacement.

Keywords: tension chord, lap splices, mechanical model, crack width, boundary element, RC walls

1 Introduction

Experimental tests on reinforced concrete (RC) walls have shown that the presence of lap splices may lead to a significant reduction of the member strength and ductility capacity (Almeida et al. 2017). The behaviour of lap splices is influenced by several factors, among which lap splice length (l_s) and confining reinforcement play a dominant role. Namely, short and poorly confined lap splices located in regions where inelastic deformations are largest (i.e. plastic hinges) may induce failure of the RC wall prior to yielding of the longitudinal reinforcement. Longer and more confined lap splices may allow the wall to develop its flexural strength, however a decrease in the deformation capacity of the structural member is often still observed. Finally, long and adequately confined lap splices will relocate the plastic hinge above the spliced zone, where the deformation capacity of the flexural hinge is limited by rupture of the reinforcement or crushing of the concrete. In all cases, damage typically starts at the wall edges (boundary elements) where the deformation demand is highest (Tarquini et al. 2017), which are also the regions first attaining failure.

Most studies in the past focused on the strength of lap splices (e.g. Orangun et al. 1977; Zuo and Darwin 2000) while significantly less research is available concerning their deformation capacity. Recently, based on an experimental programme on RC wall boundary elements, Tarquini et al. (2019) proposed an expression to estimate the average strain at failure of lap splices as a function of the lap splice length, confining reinforcement, and casting

*Correspondence: joao.almeida@uclouvain.be
[2] Institute of Mechanics, Materials and Civil Engineering, UCLouvain, Place du Levant 1 L5.05.01, 1348 Louvain-la-Neuve, Belgium
Full list of author information is available at the end of the article
Journal information: ISSN 1976-0485 / eISSN 2234-1315

Springer Open

© The Author(s) 2020. This article is licensed under a Creative Commons Attribution 4.0 International License, which permits use, sharing, adaptation, distribution and reproduction in any medium or format, as long as you give appropriate credit to the original author(s) and the source, provide a link to the Creative Commons licence, and indicate if changes were made. The images or other third party material in this article are included in the article's Creative Commons licence, unless indicated otherwise in a credit line to the material. If material is not included in the article's Creative Commons licence and your intended use is not permitted by statutory regulation or exceeds the permitted use, you will need to obtain permission directly from the copyright holder. To view a copy of this licence, visit http://creativecommons.org/licenses/by/4.0/.

position. Such expression allows estimating the deformation capacity of RC wall boundary elements with lap splices.

Past mechanical models for lap splices aimed at the characterization of their strength capacity (Priestley et al. 1996; Canbay and Frosch 2005). To the authors knowledge, the analytical model proposed by Tastani et al. (2015) is the only available in the literature describing the state of bond along spliced rebars, which can be used to predict the force–displacement response of lap splices. However, their approach is limited to the elastic response of the reinforcement bars and therefore only applicable to describe the behaviour of very short lap splice lengths (where failure will occur before any inelasticity develops in the rebars).

The present work proposes a mechanical model for the simulation of RC wall boundary elements with lap splices. It represents an extension of the tension chord model (Marti et al. 1998), reviewed in Sect. 2, which adopts the fundamental hypothesis on the constitutive materials (steel and concrete) and bond–slip laws. The model is constituted by an assembly of components, connected in series, which discretize the structural member. The three components, described in Sect. 3 are: (i) the anchorage-slip element; (ii) the basic tension chord element; and (iii) the lap splice element. The solution procedure, which concludes the same section, allows to obtain for an imposed global displacement: the steel and concrete stress and strain distributions along the boundary element, crack location and width, and the total applied axial force. Moreover, the equation proposed by Tarquini et al. (2019) for the lap splice deformation capacity can be directly employed in order to determine the failure of the spliced RC boundary element. The validation of the proposed model is carried out in Sect. 4 in terms of force–displacement, crack widths, and spliced rebar strains. Conclusions are drawn in Sect. 5.

2 Tension Chord Model

The tension chord model was originally developed as a simplified method for the determination of the rotation capacity of flexural plastic hinges in reinforced concrete girders (Sigrist and Marti 1994; Sigrist 1995). Later, it was extended to plane stress analysis problems (Kaufmann 1998; Kaufmann and Marti 1998) and to investigate the deformation capacity of prestressed and non-prestressed RC members (Alvarez 1998). It proved particularly useful in addressing problems of cracking, tension stiffening, and minimum reinforcement in RC members subjected to uniaxial loading (Marti et al. 1998). In the following paragraphs, the main assumptions and theoretical aspects underlying the tension chord model are briefly summarized.

Considering the tension chord element of Fig. 1a, the equilibrium equations for an infinitesimal length dx of concrete and steel volumes can be written as (see Fig. 1b):

$$\frac{d\sigma_c}{dx} = -\frac{\tau_b \cdot \pi \cdot \phi_l}{A_t \cdot (1-\rho_l)} \tag{1}$$

$$\frac{d\sigma_s}{dx} = \frac{4 \cdot \tau_b}{\phi_l} \tag{2}$$

where σ_c and σ_s are the concrete and steel stresses, τ_b is the bond stress, ϕ_l is the longitudinal rebar diameter, A_t is the gross sectional area, and $\rho_l = A_s/A_t$ is the longitudinal reinforcement ratio, where $A_s = \pi\phi_l^2/4$ is the steel area.

Strain–displacement relations provide $\varepsilon_s = du_s/dx$ and $\varepsilon_c = du_c/dx$, where u_s and u_c are the steel and concrete displacements, as shown Fig. 1c, and ε_s and ε_c are the corresponding strains. From compatibility considerations (Fig. 1c), the steel–concrete slip δ can be expressed as the difference between the steel and concrete displacements:

$$\delta = u_s - u_c \tag{3}$$

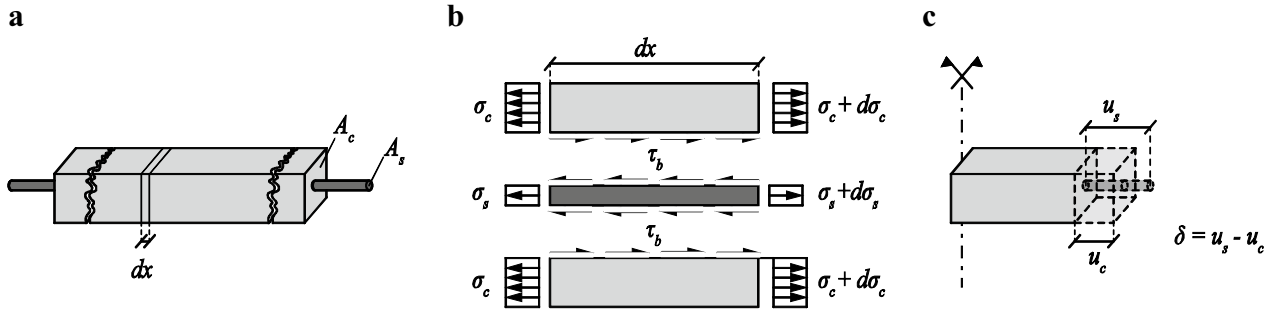

Fig. 1 After (Marti et al. 1998): **a** Sketch of a basic tension chord element, i.e. the portion of tension chord between two cracks. **b** Concrete and steel equilibrium for an infinitesimal length *dx*. **c** Compatibility requirements.

Assuming a linear and bilinear stress–strain law for the concrete and steel in tension (Fig. 2a, b), the following second order differential equation is obtained by combining the previous equations and using the chain rule of differentiation:

$$\frac{d^2\delta}{dx^2} = \frac{4 \cdot \tau_b}{d\sigma_s/dx \cdot \phi_l} + \frac{\tau_b \cdot \pi \cdot \phi_l}{A_t \cdot E_c \cdot (1 - \rho_l)} \tag{4}$$

where $d\sigma_s/dx$ and E_c are the steel and concrete tangent stiffness. Before steel yielding $d\sigma_s/dx = E_s$, while after yielding $d\sigma_s/dx = E_{sh}$, which stands for the post-yield steel stiffness.

Equation (4) can be integrated if the bond–slip (τ_b–δ) relationship is known. In the tension chord model, the latter is assumed to be stepped, rigid-perfectly-plastic (Fig. 2c): the bond stress is constant (τ_{b0}) up to reinforcement yielding, after which it halves ($\tau_{b1} = \tau_{b0}/2$). This assumption for the τ_b–δ law is particularly convenient as it allows the uncoupling of the bond stress from the slip of the reinforcing bar. In the portion between two consecutive cracks of the tension chord (herein referred as basic tension chord element), the steel stress distribution can thus be derived from the equilibrium conditions alone, i.e. without the need to resort to complex numerical integration of the above second order differential equation. As a consequence, the concrete stress, concrete strain, and steel strain distributions can also be obtained, allowing the determination of the crack width and basic tension chord elongation. In the present work, as suggested by Marti et al. (1998), it is assumed $\tau_{b0} = 2 \cdot f_{ct}$ and $\tau_{b1} = f_{ct}$, where f_{ct} is the tensile concrete strength. The latter can be computed as a fraction of the concrete cylinder strength f'_c; the calculations presented herein assume $f_{ct} = 0.3 \cdot f_c'^{2/3}$ (Sigrist and Marti 1994; Sigrist 1995).

2.1 Evolution of Deformation in a Tension Chord Subjected to Increasing Displacement

Consider a tension chord of total length L_0 (Fig. 3a) subjected to an increasing imposed tensile displacement Δ. A qualitative force–displacement response is depicted in Fig. 3b. Before first cracking, no relative slip occurs between the longitudinal steel and concrete, which thus share the same state of deformation, corresponding to state A in Fig. 3. The equivalent member axial stiffness is computed as the sum of the stiffness of the two materials:

$$\frac{(EA)_{equiv.}}{L_0} = \frac{(E_c \cdot A_c + E_s \cdot A_s)}{L_0} \tag{5}$$

where $A_c = A_t - A_s$ is the concrete area. The first crack occurs when the concrete reaches the tensile strength f_{ct} (state B in Fig. 3), which takes place at the following applied force:

$$N_{fc} = \frac{(EA)_{equiv.} \cdot f_{ct}}{E_c} \tag{6}$$

At the first forming crack the concrete stress and strain are null (state C in Fig. 3). All the applied force is taken by

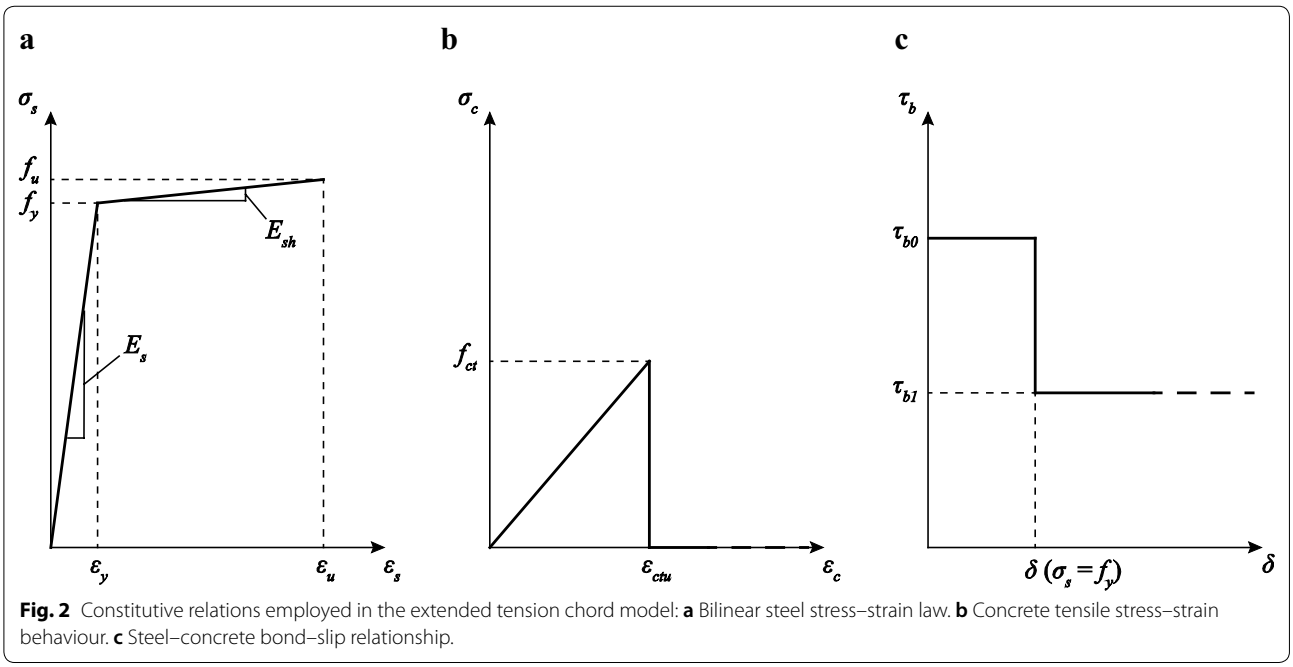

Fig. 2 Constitutive relations employed in the extended tension chord model: **a** Bilinear steel stress–strain law. **b** Concrete tensile stress–strain behaviour. **c** Steel–concrete bond–slip relationship.

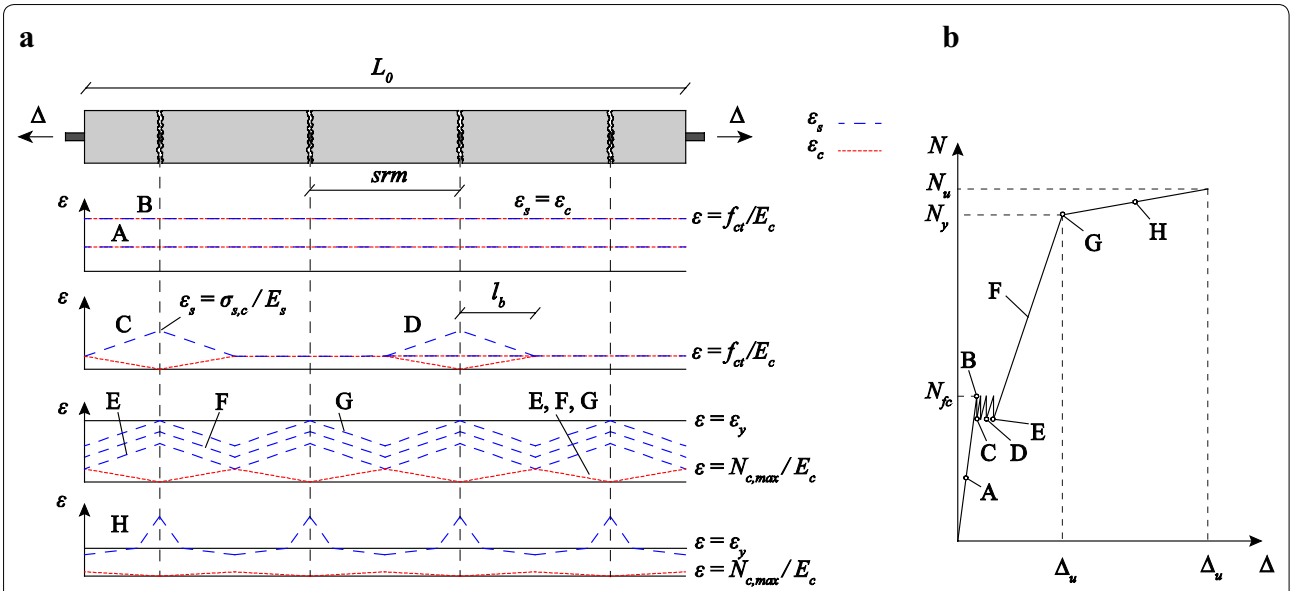

Fig. 3 Tension chord subjected to increasing imposed displacements: **a** Force–displacement response. **b** Qualitative steel and concrete strain distributions.

the longitudinal reinforcement and the steel stress passes from a pre-crack stress $\sigma_{s,B}$ to a post-crack stress $\sigma_{s,C}$. Assuming that the rebar remains elastic, which is typically the case for common ranges of longitudinal reinforcement ratios, they are computed as:

$$\sigma_{s,B} = \frac{E_s \cdot f_{ct}}{E_c} \tag{7}$$

$$\sigma_{s,C} = \frac{N_{fc}}{A_s} \tag{8}$$

For larger imposed deformations, cracks will open one after the other along the tension chord (state D in Fig. 3 refers to the opening of the second crack) up until crack stabilization. The latter corresponds to the situation in which an increase in the imposed deformation results in simple opening of existing cracks; i.e. no new cracks are forming as shown by states E, F and G in Fig. 3. The difference between the rebar force in the post-crack phase, $\sigma_{s,C}\pi\phi_l^2/4$, and the rebar force in the pre-crack state, $\sigma_{s,B}\pi\phi_l^2/4$, is transferred through bond action along a rebar surface $\pi\phi_l l_b$, which allows to express the development length l_b as (see Fig. 3a):

$$l_b = \frac{\phi_l \cdot \left(\sigma_{s,C} - \sigma_{s,B}\right)}{4 \cdot \tau_{b0}} = \frac{\phi_l \cdot f_{ct} \cdot (1 - \rho_l)}{4 \cdot \rho_l \cdot \tau_{b0}} \tag{9}$$

Two contiguous cracks cannot open at a distance greater than 2 l_b, for in such case a region between these cracks would exist where the concrete stress would be larger than the concrete tensile strength f_{ct}. On the other hand, crack spacing *srm* cannot be smaller than l_b, for it would be impossible to develop concrete stress equal to f_{ct}, even assuming a completely asymmetrical contribution of bond stress towards one of the sides. Although several expressions have been proposed in the literature to evaluate the average crack spacing *srm* (CEB 1978; FIP-CEB 1990; EN 1992-Part 1-1 2004; FIB 2013), in this paper the intermediate value of $srm = 1.5 \cdot l_b$ is assumed, which was judged to provide the compromise between simplicity (limited number of parameters) and accuracy (best final agreement with the experimental results).

The maximum force carried by the concrete, $N_{c,max}$, depends on the value of *srm* and can be computed as:

$$N_{c,max} = \frac{srm}{2} \cdot \tau_{b0} \cdot \phi_l \cdot \pi \tag{10}$$

In between two cracks, the steel and concrete stress and strain distributions can be obtained by solving analytically Eq. (4). The crack width w is then calculated as the integral along *srm* of the difference between the steel and concrete strains—Eq. (11)—while the integral of the steel strains gives the total elongation of the basic tension chord—Eq. (12).

$$w = \int_{-\frac{srm}{2}}^{\frac{srm}{2}} \varepsilon_s - \varepsilon_c dx \tag{11}$$

$$\Delta_{TC} = \int_{-\frac{srm}{2}}^{\frac{srm}{2}} \varepsilon_s dx \tag{12}$$

For the assumed material and bond–slip relationships, in-between cracks the steel and concrete stress and strain distributions remain linear up to yielding of the longitudinal reinforcement (state G in Fig. 3). After yielding, the reduction of the steel tangent stiffness (from E_s to E_{sh}) and bond stress (from τ_{b0} to τ_{b1}) causes the shift from linear to bilinear stress and strain distributions, as represented in state H of Fig. 3a.

3 Mechanical Model for Boundary Elements of RC Walls with Lap Splices

The mechanical model proposed in the following is developed to simulate the response of RC wall boundary elements with lap splices, subjected to a uniaxial tension–compression loading. It is an extension of the classical tension chord model (Marti et al. 1998) described in the previous section. The basic tension chord element is used in series with an anchorage-slip element and a newly developed lap-splice element; they are described in the next three Sects. 3.1 to 3.3. Section 3.4 deals instead with the iterative solution strategy employed to obtain local deformations and forces for an imposed global displacement.

3.1 Anchorage-Slip Element

The deformation of RC walls due to strain penetration of the longitudinal reinforcement in the foundation can represent an important contribution to the total member displacement (Zhao and Sritharan 2007; Sousa et al. 2018). The anchorage-slip element presented herein allows to estimate the anchorage-slip displacement Δ_{anc} as well as to determine the steel and concrete stress and strain distributions along the anchorage length l_{anc}. The input parameter is the steel strain at the loaded end, ε_{ac}, where the subscript *ac* stands for '*at crack*' as it corresponds to the location of the RC wall-foundation interface crack. It is assumed that the rebar capacity cannot crack the foundation and that concrete strains are negligible compared to steel strains, which is typically the case. The elongation Δ_{anc} can again be computed as the integral of the steel strains:

$$\Delta_{anc} = \int_{l_{anc}} \varepsilon_s dx \tag{13}$$

Building on the material and bond assumptions described in the previous section, analytical expressions for Δ_{anc} can be derived, which depend on the anchorage type (straight or bent rebars), anchorage length, and imposed free-end deformation ε_{ac}. For a review of the different cases, the reader is referred to Feng and Xu (2018), where a full description of the equations for the calculation of Δ_{anc} can be found. The current work only considers the anchorage configuration featured by the test units used to carry out the model validation in Sect. 4; i.e., rebars bent inside the foundation and an anchorage length l_{anc} longer than the development length required to achieve the ultimate steel stress (l_{ult}). For bent rebars, l_{anc} can be evaluated as a function of the straight portion of the anchored length l_0 (Sezen and Setzler 2008):

$$l_{anc} = l_0 + 5 \cdot \phi_l \tag{14}$$

while l_{ult}, composed by elastic and plastic components (l_y and l_p respectively), can be computed as:

$$l_{ult} = l_y + l_p = \frac{f_y \cdot \phi_l}{4 \cdot \tau_{b0}} + \frac{(f_u - f_y) \cdot \phi_l}{4 \cdot \tau_{b1}} \tag{15}$$

where f_y and f_u are the steel yield and ultimate strength. The analytical expression to calculate the slip Δ_{anc} in case of $l_{anc} > l_{ult}$ is given by the following equation:

$$\Delta_{anc} = \begin{cases} \frac{\varepsilon_{ac}}{2} \cdot l_{ac} & for\ \varepsilon_{ac} < \varepsilon_y \\ \frac{\varepsilon_y}{2} \cdot l_y + \frac{\varepsilon_y + \varepsilon_{ac}}{2} \cdot (l_{ac} - l_y) & for\ \varepsilon_{ac} > \varepsilon_y \end{cases} \tag{16}$$

where l_{ac} is the development rebar length required to attain the strain at crack ε_{ac}, and is computed as:

$$l_{ac} = \begin{cases} \frac{\varepsilon_{ac} \cdot E_s \cdot \phi_l}{4 \cdot \tau_{b0}} & for\ \varepsilon_{ac} < \varepsilon_y \\ \frac{f_y \cdot \phi_l}{4 \cdot \tau_{b0}} + \frac{(\varepsilon_{ac} - \varepsilon_y) \cdot E_{sh} \cdot \phi_l}{4 \cdot \tau_{b1}} & for\ \varepsilon_{ac} > \varepsilon_y \end{cases} \tag{17}$$

The previous expressions underline that pre- and post-yielding cases are distinguished; for each case, a sketch of the qualitative steel stress and strain distributions is included in Fig. 4.

The upper and lower domain boundaries of applicability for Eqs. (16) and (17) are defined by the minimum steel strain required to have crack stabilization (ε_{cs}, see Sect. 3.4 for its calculation) and the ultimate steel strain (ε_{ult}), respectively. In fact, for $\varepsilon_{ac} < \varepsilon_{cs}$ the RC wall boundary element remains uncracked, implying $\Delta_{anc} = 0$. On the other hand, steel rupture will occur for $\varepsilon_{ac} > \varepsilon_{ult}$, thus resulting in the total loss of the member axial load capacity ($N = 0$).

3.2 Basic Tension Chord Element

As introduced in the previous section, the basic tension chord element represents the portion of a tension chord enclosed between two consecutive cracks (spaced *srm* apart). For an arbitrary value of $\varepsilon_{cs} < \varepsilon_{ac} < \varepsilon_{ult}$, where ε_{ac} is the steel strain at crack, the steel and concrete stress and strain distributions can be determined by equilibrium considerations. The crack width as well as the total chord elongation are obtained by applying Eqs. (11) and (12), respectively. Three cases can be distinguished: (i) $\varepsilon_{ac} < \varepsilon_y$; (ii) $\varepsilon_{ac} > \varepsilon_y$ and $l_{ac,p} < srm/2$; and (iii) $\varepsilon_{ac} > \varepsilon_y$ and

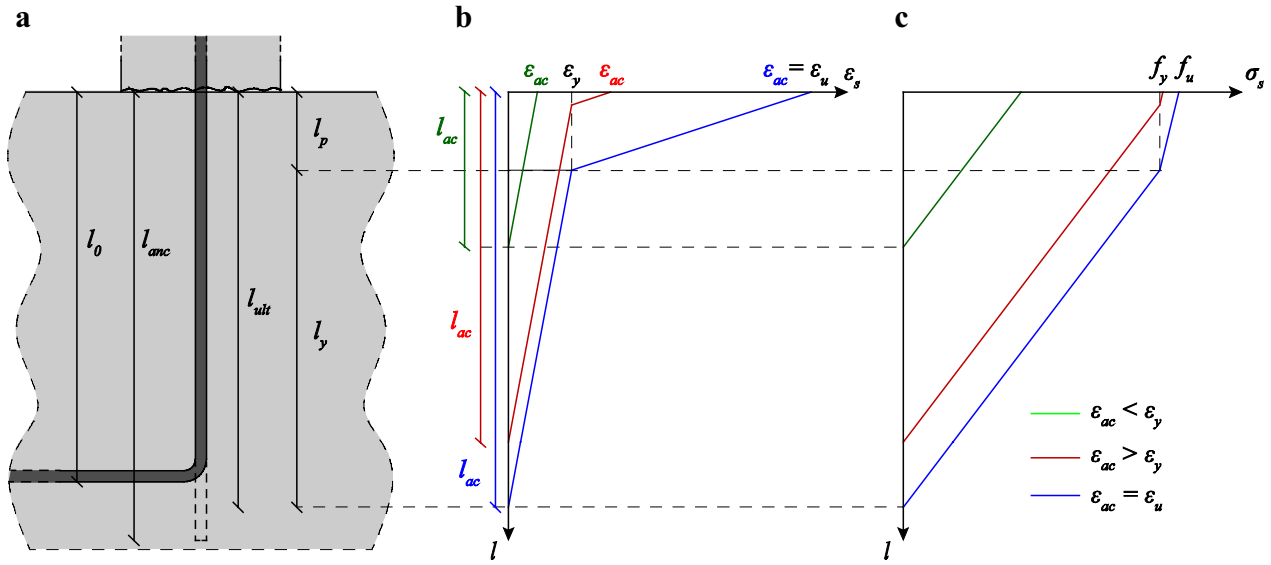

Fig. 4 Anchorage-slip element for bent anchored bars with $l_{anc} > l_{ult}$: **a** Sketch of the anchorage detail. **b** Qualitative steel strain profiles. **c** Qualitative steel stress profiles.

$l_{ac,p} > srm/2$, where $l_{ac,p}$ is the length required to develop the plastic strain $\varepsilon_p = \varepsilon_{ac} - \varepsilon_y$, computed as:

$$l_{ac,p} = \frac{A_s \cdot E_{sh} \cdot (\varepsilon_{ac} - \varepsilon_y)}{\tau_{b1} \cdot \pi \cdot \phi_l} \tag{18}$$

For each case, the material stress and strain distribution is depicted in Fig. 5, while the expression for calculating the basic chord elongation Δ_{TC} and the crack width w are provided by Eqs. (19) and (20), obtained by solving Eqs. (11) and (12):

$$\Delta_{TC} = \begin{cases} \left(\varepsilon_{ac} - \frac{N_{c,max}}{2 \cdot A_s \cdot E_s}\right) \cdot srm & for\ case(i) \\ \varepsilon_{ac} \cdot l_{ac,p} + \varepsilon_y \cdot \frac{srm}{2} + \varepsilon_{srm/2} \cdot \left(\frac{srm}{2} - l_{ac,p}\right) & for\ case(ii) \\ \left(\varepsilon_{ac} - \frac{N_{c,max,p}}{2 \cdot A_s \cdot E_{sh}}\right) \cdot srm & for\ case(iii) \end{cases} \tag{19}$$

$$w = \begin{cases} \left(\varepsilon_{ac} - \frac{N_{c,max}}{2 \cdot A_s \cdot E_s} - \frac{N_{c,max}}{2 \cdot A_c \cdot E_c}\right) \cdot srm & for\ case(i) \\ \Delta_{TC}^{case(ii)} - \varepsilon_{c,y} \cdot \frac{srm}{2} - \varepsilon_{c,srm/2} \cdot \left(\frac{srm}{2} - l_{ac,p}\right) & for\ case(ii) \\ \left(\varepsilon_{ac} - \frac{N_{c,max,p}}{2 \cdot A_s \cdot E_{sh}} - \frac{N_{c,max,p}}{2 \cdot A_c \cdot E_c}\right) \cdot srm & for\ case(iii) \end{cases} \tag{20}$$

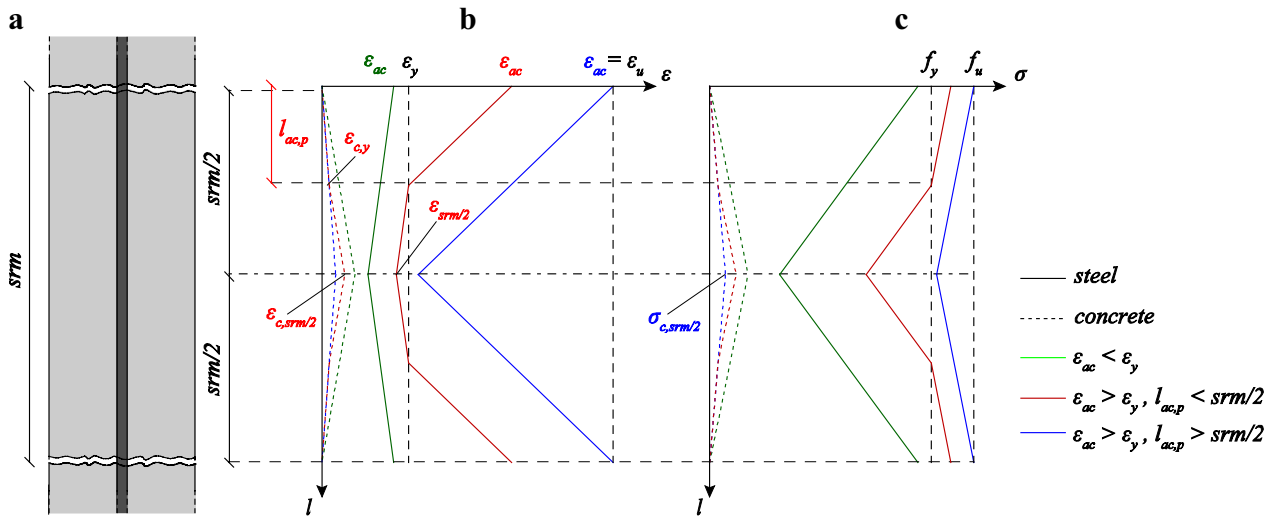

Fig. 5 Basic tension chord element: **a** Sketch. **b** Qualitative steel and concrete strain profile. **c** Qualitative steel and concrete stress profile.

where $\varepsilon_{srm/2}$ and $\varepsilon_{c,srm/2}$ are the steel and concrete strains evaluated at $srm/2$, Eqs. (21) and (22); $\varepsilon_{c,y}$ is the concrete strain in correspondence of the steel yield point, Eq. (23); and $N_{c,max,p}$ is the maximum concrete force occurring at $srm/2$ when the steel is in the post-yield state, Eq. (24).

$$\varepsilon_{srm/2} = \varepsilon_y - \frac{\tau_{b0} \cdot \pi \cdot \phi_l \cdot \left(\frac{srm}{2} - l_{ac,p}\right)}{A_s \cdot E_s} \tag{21}$$

$$\varepsilon_{c,srm/2} = \varepsilon_{c,y} + \frac{\tau_{b0} \cdot \pi \cdot \phi_l \cdot \left(\frac{srm}{2} - l_{ac,p}\right)}{A_c \cdot E_c} \tag{22}$$

$$\varepsilon_{c,y} = \frac{\tau_{b1} \cdot \pi \cdot \phi_l \cdot l_{ac,p}}{A_c \cdot E_c} \tag{23}$$

$$N_{c,max,p} = \sigma_{c,max,p} \cdot A_c = \frac{srm}{2} \cdot \tau_{b1} \cdot \phi_l \cdot \pi \tag{24}$$

3.3 Lap-Splice Element

As outlined above, the strength and/or deformation capacity of RC walls may be sensibly reduced by the presence of lap splices above the foundation level, where the seismic demand is maximum. Adequate detailing, i.e. providing appropriate lap-splice length and confining reinforcement, is crucial in order to attain the desired member ductility. The component presented in this subsection allows to account for the presence of lap splices in RC wall boundary elements and to estimate: (i) the steel strain distribution in the pair of spliced rebars; (ii) the crack width along the lap-splice length as well as the width contribution to the splice-end cracks originating from lap-splice deformation; (iii) the total lap-splice displacement and the failure point.

This component builds on the same hypothesis regarding material and bond behaviour assumed for the tension chord model described in Sect. 2. Once crack stabilization is attained along the lap-splice length (Fig. 6a), the resisting force is transferred from the anchored to the free end (unloaded) rebar through concrete bond. It is herein assumed that the concrete remains undeformed while transferring the force from one bar to another. Although the applied tensile load is partly resisted by the concrete, causing the formation of splitting cracks, the previous simplification represents a reasonable approximation up to the point of lap splice failure. In fact, as pointed out by Tastani et al. (2015), neglecting the concrete strain contribution does not result in large model errors since the maximum tensile strain carried by normal strength-concrete up to tensile failure is less than 5% of the yield strain of the reinforcement. Nevertheless, this hypothesis implies a slight overestimation of the crack width as the latter is computed from the steel deformations alone, i.e. the tension stiffening effect due to concrete strains is ignored. A qualitative sketch of the steel stress and strain distribution for the couple of spliced rebars is represented in Fig. 6b, c for two different levels of strain at the interface crack ε_{ac} (pre- and post-yielding). From the top interface crack downwards, the steel stress is progressively transferred from the top-anchored to the bottom-anchored rebar. The stress transfer stops when equilibrium is reached with the two rebars attaining the same force level. An analogous if mirrored physical phenomenon occurs on the bottom half of the lap splice.

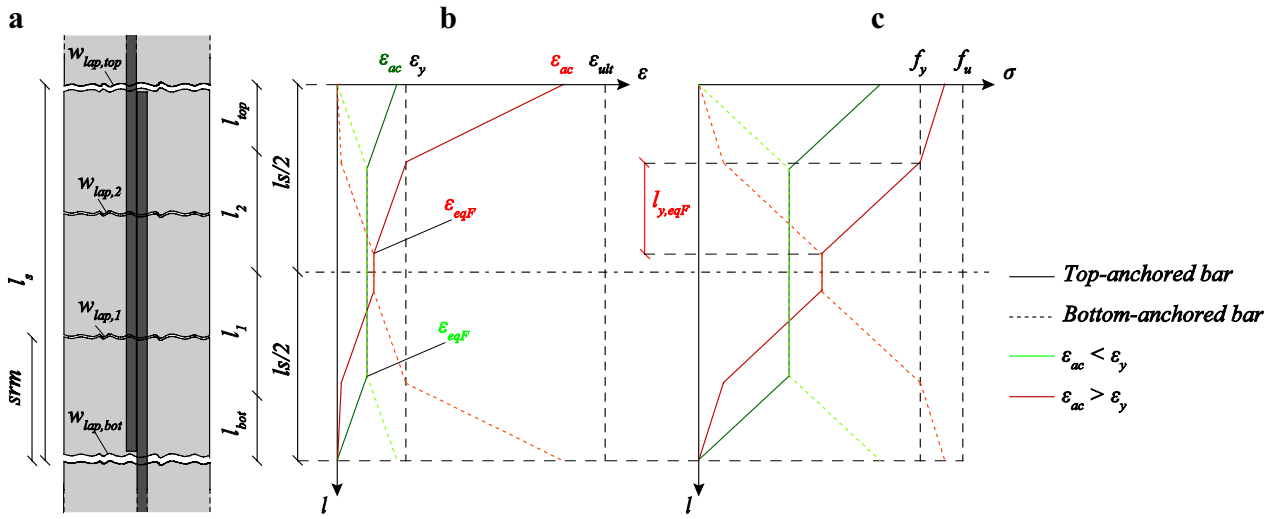

Fig. 6 Lap-splice element: **a** Sketch. **b** Qualitative steel strain profile. **c** Qualitative steel stress profile.

The crack spacing *srm* within the lap-splice zone is assumed the same as outside, which is supported by experimental observations. The width of the cracks located within the lap-splice region (for instance $w_{lap,1}$ and $w_{lap,2}$ in Fig. 6a) is computed by integrating, along the corresponding influence length (e.g. l_1 and l_2 in Fig. 6a), the envelope (i.e., the maximum) of the strains along the spliced rebars. For a given crack, the influence length is taken as the sum of the two half distances from the contiguous upper and lower cracks. Similarly, the integral of the strain envelopes along l_{top} and l_{bot} (see Fig. 6a) provide the portion of the top and bottom interface crack widths due to deformations originating within the lap splice region. The total width of these cracks is then obtained by summing up the contributions due to deformations occurring within and outside the lap splice region (the next subsection provides further details). The steel strain envelope is considered for the calculation of the crack width because, along the lapped zone, the spliced rebars are in general not equally stressed; the more stressed bar governs crack width (Tastani et al. 2015). Closed-form expressions for the calculation of the splice-internal crack widths and the contribution to the interface cracks given by deformations within the lap-splice region are relatively complicated to obtain as they depend on a large number of variables. Therefore, in the present study these widths are computed numerically.

The total lap splice displacement (Δ_{ls}) is calculated as the integral of the steel strain envelopes along the entire lap splice length: the expressions for both the elastic ($\varepsilon_{ac} < \varepsilon_y$) and post-yield ($\varepsilon_{ac} > \varepsilon_y$) cases are as follows:

$$\Delta_{ls} = \begin{cases} \frac{1}{4}\varepsilon_{ac}(2 \cdot l_s - l_{ac}) & \varepsilon_{ac} < \varepsilon_y \\ (\varepsilon_{ac} - \varepsilon_y) \cdot l_{ac,p} + (\varepsilon_y + \varepsilon_{eqF}) \cdot l_{y,eqF} + 2 \cdot \varepsilon_{eqF} \cdot \left(\frac{l_s}{2} - l_{ac,p} - l_{y,eqF}\right) & \varepsilon_{ac} > \varepsilon_y \end{cases} \quad (25)$$

where ε_{eqF}, Eq. (26), is the strain of both top and bottom anchored rebars when they share the same force, and $l_{y,eqF}$ is the distance between the yield point and the first point in which ε_{eqF} is reached, see Fig. 6b.

$$\varepsilon_{eqF} = \frac{E_{sh} \cdot (\varepsilon_{ac} - \varepsilon_y) + E_s \cdot \varepsilon_y}{2 \cdot E_s} \quad (26)$$

$$l_{y,eqF} = \frac{A_s \cdot (E_s \cdot \varepsilon_y - E_{sh} \cdot (\varepsilon_{ac} - \varepsilon_y))}{2 \cdot \tau_{b0} \cdot \pi \cdot \phi_l} \quad (27)$$

Based on experimental data on uniaxial cyclic tests on spliced RC members, Tarquini et al. (2019) determined an expression for the average strain at lap splices failure (ε_{ls}). The latter, which depends on lap splice length, amount of confinement reinforcement and casting position, is used in the proposed model to define the deformation capacity of lap splices. The ultimate lap-splice displacement ($\Delta_{ls,ult}$) is therefore straightforwardly obtained by multiplying ε_{ls} by the nominal lap-splice length l_s; failure of the lap-splice element is assumed to take place at this point, with the complete loss of the axial load capacity. It is worth noticing that the above-mentioned failure criterion typically precedes the attainment of non-zero stress values at the lap splice free ends ($l_{ac} > l_s$). In such a case, pull-out rather than lap splice failure might be expected.

3.4 Model implementation: iterative procedure and failure criteria

The components described in the three previous subsections can be connected in series in order to simulate the response of RC wall boundary elements with lap splices subjected to increasing tensile loading. Figure 7a illustrates the assembly of an anchorage, lap splice, and several basic tension chord elements, to which a global top displacement Δ_{tot} is imposed. Given the steel and concrete material properties, outputs of the model are the resisting axial force, crack spacing and widths (inside and outside the lap-splice region), steel and concrete strain distributions, and the ultimate displacement. Iterations are required to solve the nonlinear problem, unless global forces are imposed, wherein a straightforward non-iterative solution is available. A flowchart depicting the steps involved in the iterative procedure is illustrated in Fig. 7b and discussed in the following paragraph.

Up to first cracking, perfect bond exists between steel and concrete, which therefore share the same strain:

$$\varepsilon_s = \varepsilon_c = \frac{\Delta_{tot}}{L_0} \quad (28)$$

where L_0 represents the total length of the boundary element (see Fig. 7a). First cracking occurs at a displacement level $f_{ct}L_0/E_c$ with N_{fc} given by Eq. (6). Between first cracking and crack stabilization (identified by the subscript '*cs*'), cracks open one after the other with the axial force that is assumed constant and equal to $N = N_{fc}$. In reality, small force drops occur due to the stiffness reduction caused by each crack opening, as shown in Fig. 3. The displacement at crack stabilization Δ_{cs} is identified by a steel strain at crack equal to:

$$\varepsilon_{cs} = \frac{N_{fc}}{E_s \cdot A_s} \quad (29)$$

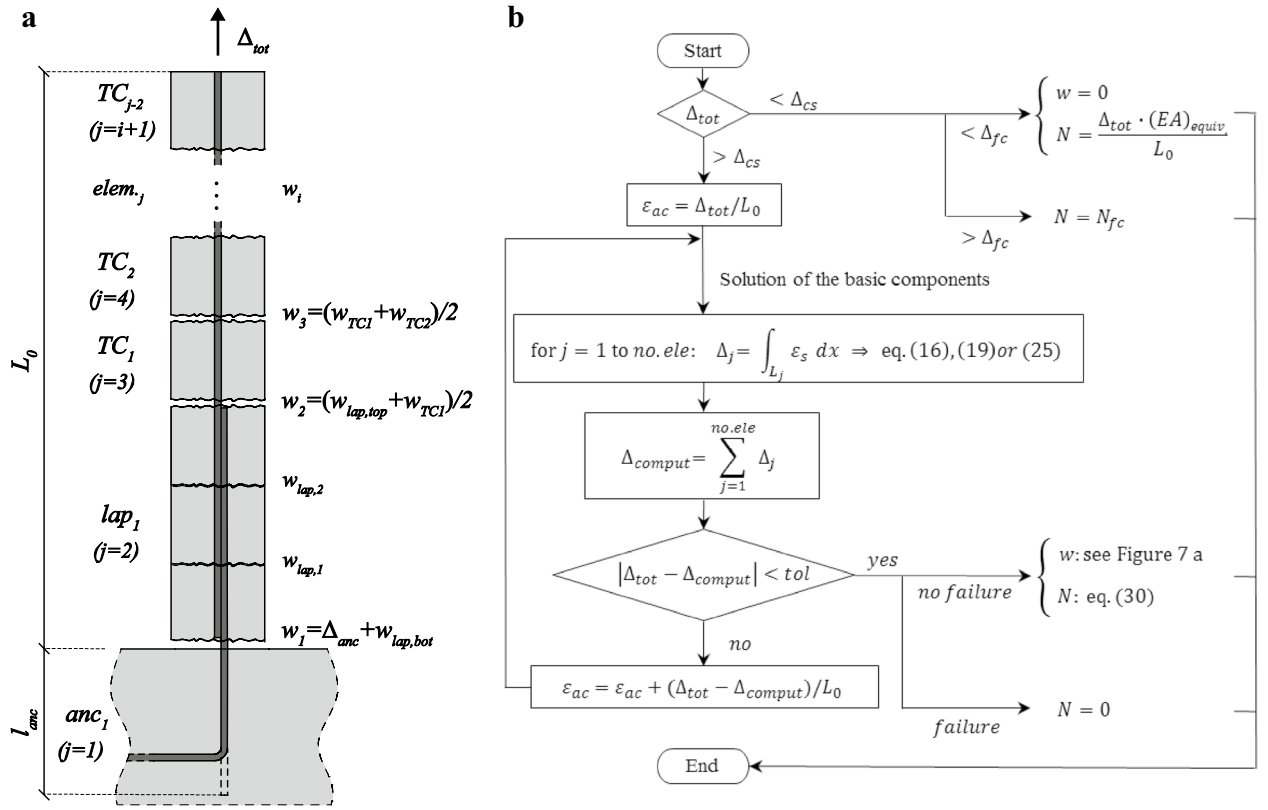

Fig. 7 RC boundary element model: **a** Assembly of the components for a RC member featuring lap splice, anchorage, and multiple basic tension chord (TC_i) elements. **b** Flowchart of the iterative procedure.

The above does not apply to cracks located within the lap-splice region where the steel area contributing to the axial stiffness is double. Such cracks open at an imposed axial force $N_{fc,lap} > N_{fc}$; however, for common longitudinal reinforcement ratios the difference between the two forces is relatively small and can be neglected (e.g., for the case-study of Sect. 4, $N_{fc,lap} = 140$ kN while $N_{fc} = 130$ kN).

For imposed displacements larger than Δ_{cs}, each component of the boundary element (anchorage, lap splice, and basic tension chord) can be solved separately for a given strain at crack ε_{ac}. This quantity is initially estimated as $\varepsilon_{ac} = \Delta_{tot}/L_0$ which is then used to compute the resulting total boundary element displacement. The latter, identified as Δ_{comput}, is obtained by summing up the resulting displacement of each element, evaluated through Eqs. (16), (19), and (25). The computed displacement Δ_{comput} is then compared to the externally imposed Δ_{tot}: if their difference is smaller than a user-defined tolerance (in the following applications $tol = \Delta_{tot}/1000$ is used), convergence is attained, otherwise an updated estimate of ε_{ac} is calculated (see Fig. 7b) and a new iteration is performed. At convergence, the steel/concrete stress/strain distributions can be retrieved from each element, as well as the crack widths (see Fig. 7a). Finally, the total imposed axial force is calculated as:

$$\begin{cases} N = \varepsilon_{ac} \cdot E_s \cdot A_s & \varepsilon_{ac} < \varepsilon_y \\ N = \varepsilon_y \cdot E_s \cdot A_s + (\varepsilon_{ac} - \varepsilon_y) \cdot E_{sh} \cdot A_s & \varepsilon_{ac} > \varepsilon_y \end{cases} \tag{30}$$

Without a specific criterion defining the failure of the boundary element, the procedure above can be performed for any imposed displacement Δ_{tot} up to a strain at crack equal to the ultimate steel strain ($\varepsilon_{ac} = \varepsilon_{ult}$). The latter represents a reasonable failure criterion only in case of continuous reinforcement and monotonic tensile loading. In case of cyclic loading and continuous reinforcement, the ultimate steel strain will result in an overestimation of the member displacement capacity and a value of $\varepsilon_s = 0.6\ \varepsilon_{ult}$ can be used (Priestley et al. 2007). In case lap splices are also present, the attainment of the aforementioned ultimate displacement of the lap splice element, $\Delta_{ls,ult}$, signals the member failure, which consists in the total and sudden loss of the axial load carrying capacity.

4 Validation of the Proposed Model

Results from a recently concluded experimental programme on RC wall boundary elements with lap splices (Tarquini et al. 2018) are used to validate the proposed mechanical model. The 24 test units (TUs), of which 22 with lap splices and two reference units with continuous reinforcement, shared the same geometry, illustrated in Fig. 8. They differed in terms of lap-splice length, confining reinforcement and loading history, which constituted the variable parameters of the test programme. The testing machine was a uniaxial press with a fixed top and a mobile bottom actuator to which the TUs were connected by means of rigid steel profiles. The instrumentation included load-cells as well as LVDTs and LED grids to evaluate global and local displacement values. Namely, LEDs were also directly glued on the pair of spliced rebars, allowing a direct monitoring of rebar strains.

The same reinforcing steel was used for all the TUs. Although different castings were performed, the concrete showed a limited variability in the cylinder compressive strength f'_c. All details regarding material properties can be found in Tarquini et al. (2018); Table 1 reports the material parameters relevant to the mechanical model that were used to run the analyses shown in the next two subsections.

4.1 TU with Continuous Reinforcement

The mechanical model is compared in this section with the test unit LAP-C1 featuring continuous longitudinal reinforcement and a confinement reinforcement ratio $\rho_t \approx 0.3\%$. The experimental vs numerical force–displacement curves are shown in Fig. 9a with grey and black solid lines, respectively. The applied axial force N is reported on the vertical axis while the total vertical displacement Δ is given on the horizontal axis. A black

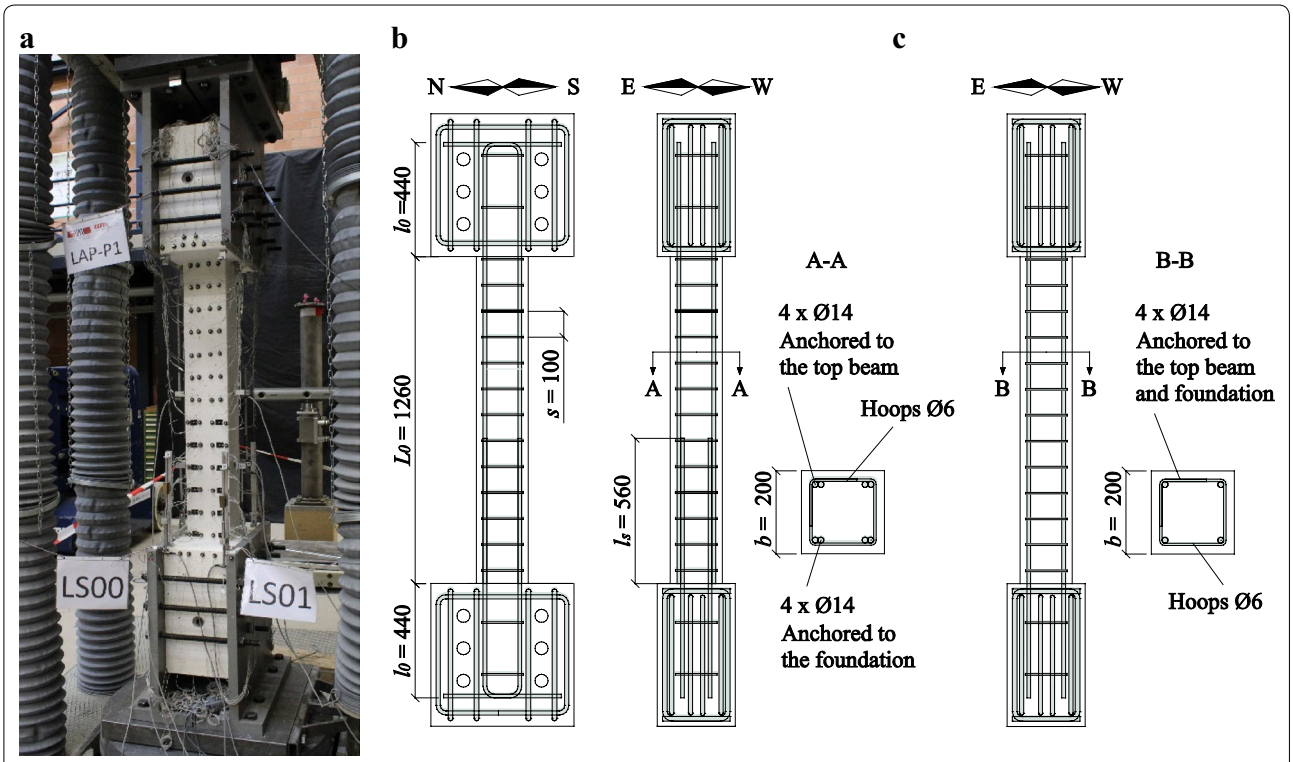

Fig. 8 Experimental programme used for model validation (Tarquini et al. 2018): **a** Photo of test unit LAP-P1 in test stand; Example of a reinforcement layout of (**b**) a TU with lap splices (LAP-P1); and (**c**) a TU with continuous reinforcement (LAP-C1).

Table 1 Material parameters used in the simulation, obtained from material tests (see Tarquini et al. 2018).

Material property	f'_c [MPa]	f_y [MPa]	f_u [MPa]	E_s [MPa]	E_{sh} [MPa]	ε_{ult} [%]
	32	510	635	204,000	1430	9

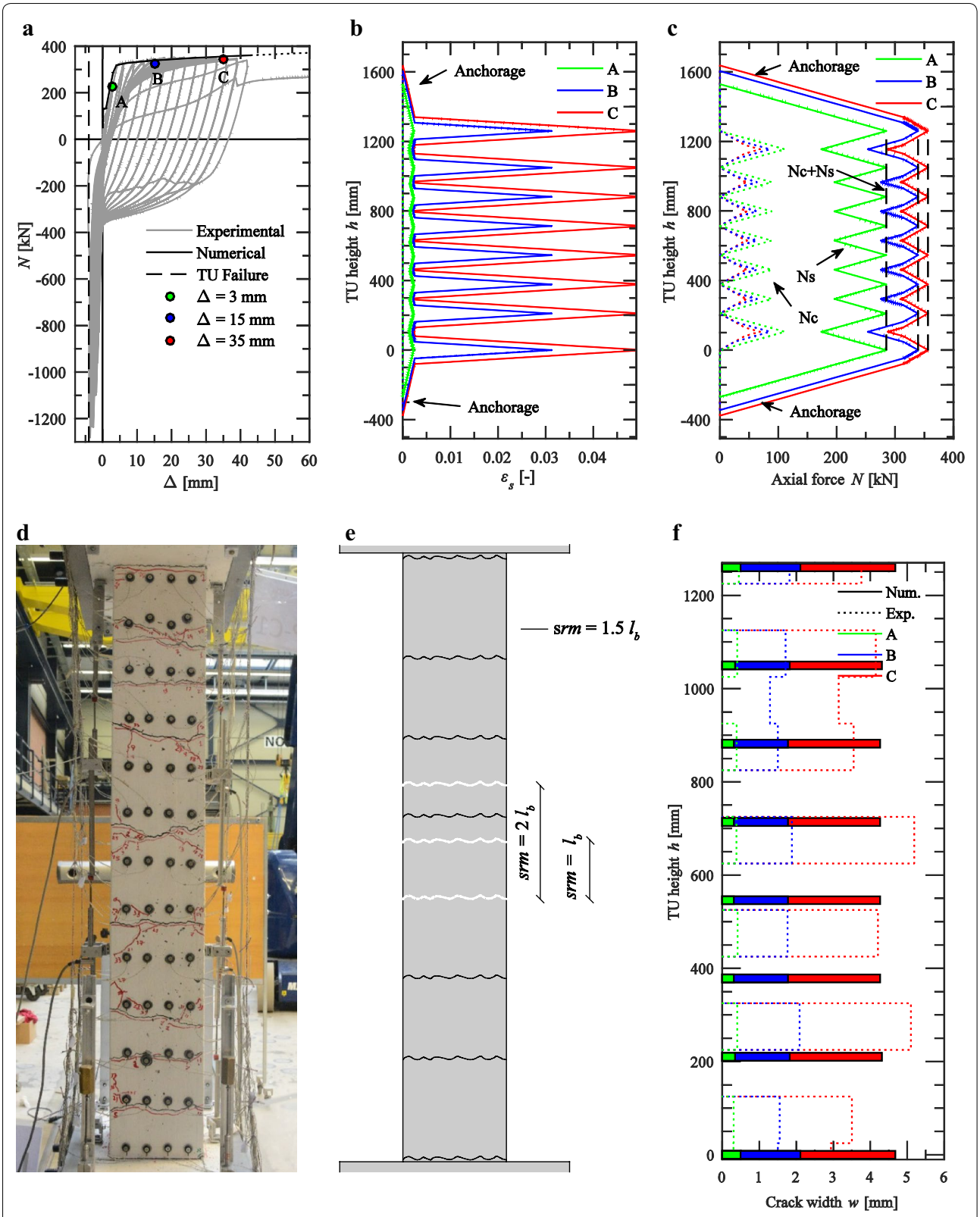

Fig. 9 Example of a test unit with continuous reinforcement (TU LAP-C1): **a** Experimental vs numerical force–displacement response. **b** Simulated steel strain profile. **c** Simulated steel and concrete force profiles. **d** Photo of crack pattern. **e** Numerical crack pattern obtained for different *srm* to l_b ratios. **f** Experimental vs numerical crack width.

dashed line indicates the displacement at which the experimental specimen failed, defined as the displacement at which a loss of axial load capacity of 20% was observed. For LAP-C1, this occurred in compression, due to core concrete crushing. The numerical pushover curve reproduces satisfactorily the tensile experimental backbone curve. Namely, the stiffness evolution as well as the maximum force are well predicted. Due to the failure in compression of the specimen, no failure criterion was defined for the mechanical model, which thus does not show decay in strength. Three coloured dots identify post-cracking ($\Delta = 3$ mm), plastic ($\Delta = 15$ mm), and pre-failure ($\Delta = 35$ mm) states, which are used in the following plots to compare local-level quantities.

Simulated steel and concrete strain distributions along the boundary element are depicted in Fig. 9b with solid and dashed lines, respectively. Steel strains were not directly measured in TUs with continuous reinforcement and therefore a comparison between numerical and experimental data is not possible. The numerically obtained distributions are well established and have been presented in several studies on the tension chord model (e.g. Kaufmann 1998; Marti et al. 1998; Muttoni and Fernandez 2010). Steel strains are maximum at crack locations, minimum midway between cracks, and increase from the post-cracked state A to the pre-failure state C. A similar trend can be observed for the steel force distribution (N_s) illustrated in Fig. 9c; on the other hand, concrete forces (N_c) show an opposite behaviour with $N_c = 0$ at crack and $N_c = N_{c,max}$ midway between cracks. Furthermore, due to the reduction in bond strength after the occurrence of reinforcement yielding, N_c between cracks decreases with the spread of inelasticity.

The discretization of the boundary element is shown in Fig. 9e and consists in two anchorage and seven basic tension chord elements, corresponding to a crack spacing $srm = 1.5 \cdot l_b$. The same figure also includes, for comparison purposes, the minimum and maximum theoretical crack spacing ($srm = l_b$ and $srm = 2 \cdot l_b$), whereas the real crack pattern observed during the test is reported in Fig. 9d.

Finally, experimental and numerical crack widths are compared, for the three levels of displacement A, B and C, in Fig. 9f. Experimental values, computed as displacement difference between markers located on the same vertical line, are represented with a dotted line, whereas numerical values are displayed in the form of bar plots at crack location. It is found that the model describes satisfactorily the experimental results for all considered displacement levels, concerning both cracks along the TU as well as foundation/top beam interface cracks. Namely, as it will be shown in Fig. 11b, the model error associated to the simulation of the average crack width is smaller than 5%.

4.2 TUs with Lap Splices

In Fig. 10, results from the mechanical model are compared against experimental data obtained from three TUs with lap splices differing in terms of both lap splice length (l_s) and confining reinforcement ratio (ρ_t). In particular, LAP-P4 had the shortest lap-splice length, $l_s = 350$ mm ($25 \cdot \varnothing_l$) and $\rho_t \approx 0.3\%$, followed by LAP-P16, $l_s = 560$ mm ($40 \cdot \varnothing_l$) and $\rho_t \approx 0.2\%$, whereas the longest lap-splice length was part of LAP-P5, $l_s = 840$ mm ($60 \cdot \varnothing_l$) and $\rho_t \approx 0.1\%$. Differently from the model used to simulate the TU with continuous reinforcement, the one used in the present subsection included a lap-splice element above the bottom anchorage element.

From shorter to longer lap splice lengths, the comparison in terms of global force–displacement is shown in in plots (a), (d) and (g). In all three cases, the numerical pushover follows satisfactorily the tensile backbone curve of the cyclic experimental results. Moreover, the ultimate displacement capacity is also rather well predicted (relative error below 20%); the numerical failure is triggered by the attainment of the ultimate lap-splice displacement. For each state (A, B, C) represented by a coloured dot in the force–displacement curves, plots (b), (e) and (h) display the numerical vs experimental crack width. A good match between the two quantities can be observed, the model being able to capture the crack evolution as well as the different openings of cracks within and outside the lap-splice region. Namely, the former are considerably smaller than the latter and the difference in crack width increases with the spread of inelasticity. The distribution of rebar steel strains along the lap splice length is also adequately simulated by the model. In plots (c), (f) and (i), the bottom-anchored rebar of the spliced pair is considered for comparison (the top anchored rebar would show similar but mirrored results). A good fit is again apparent for the three lap-splice lengths, which validates the model assumption of neglecting the concrete deformations within the lap-splice region. No comparison could be performed close to the two splice-end cracks, where steel deformations are maximum, since no strain measure was available at that location. It should also be noted that the effects of cyclic steel strength degradation and cyclic bond strength degradation are not taken into account in the model, which can contribute to explain some of the differences observed with respect to the experimental results, namely between states B and C. However, in view of the overall good agreement, it is believed that these effects were relatively limited.

In order to further validate the proposed mechanical model, the entire set of RC wall boundary elements tested by Tarquini et al. (2018) was simulated. The results are summarized in Fig. 11 in terms of relative error

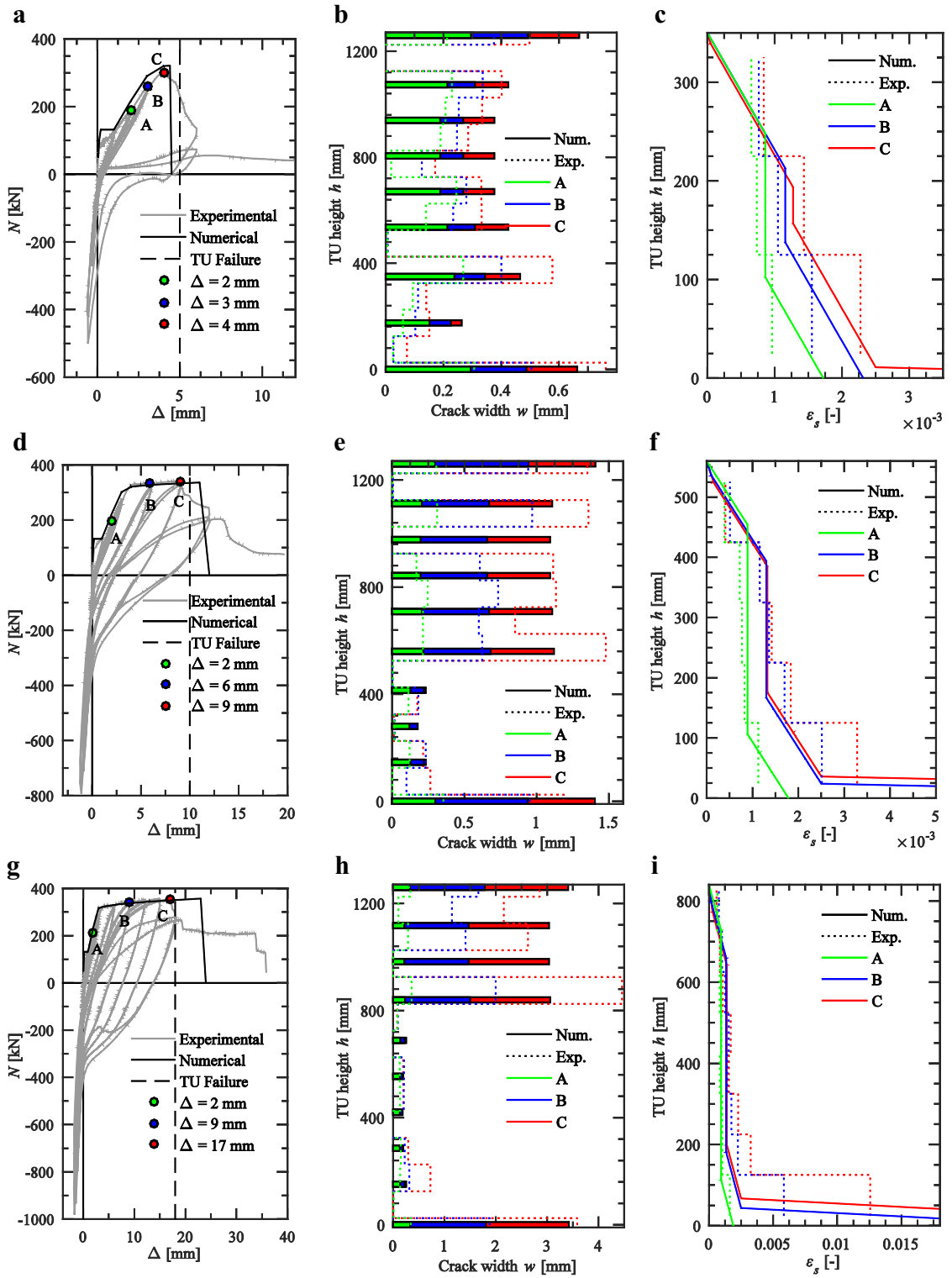

Fig. 10 Examples of test units with spliced reinforcement: Experimental vs numerical comparison for TU LAP-P4 ($l_s = 25\ \varnothing_l$), LAP-P16 ($l_s = 40\ \varnothing_l$) and LAP-P5 ($l_s = 60\ \varnothing_l$): **a**, **d**, **g** Force–displacement response. **b**, **e**, **h** Crack width. **c**, **f**, **i** Steel strains within the lap-splice region for the bottom anchored rebar.

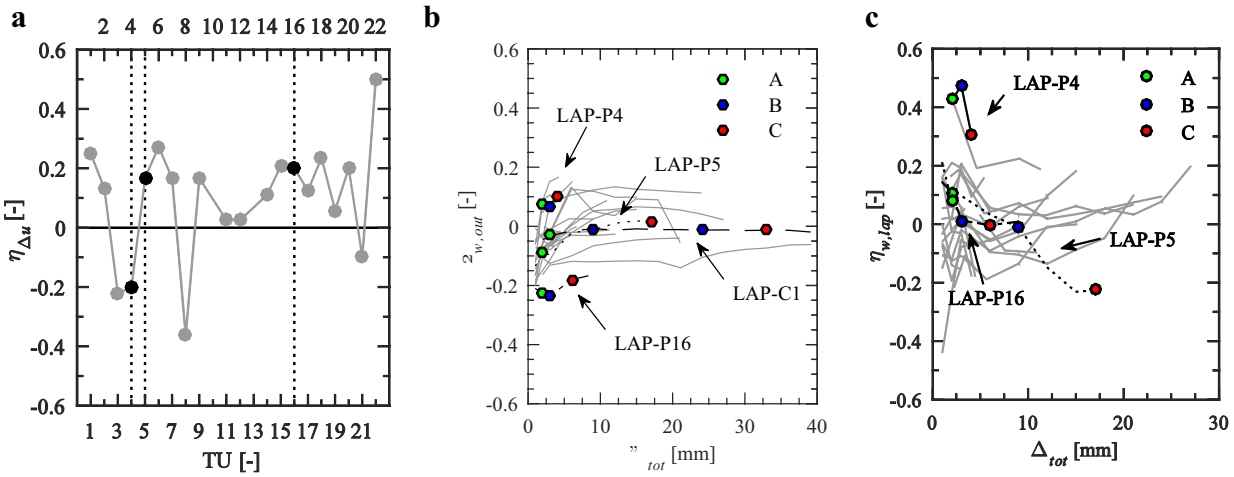

Fig. 11 Relative error for the simulation of all test units: **a** Ultimate element displacement. **b** Average crack width outside the lap-splice region. **c** Average crack width in the lap-splice region.

concerning the prediction of: (a) the failure displacement; (b) the average crack width outside the lap splice region; and (c) the average crack width within the lap splice region. The relative error η is expressed by the following equation:

$$\eta = \frac{\upsilon_{num} - \upsilon_{exp}}{\upsilon_{exp}} \tag{31}$$

where υ_{num} and υ_{exp} represent the considered numerical and experimental quantities, respectively.

From Fig. 11a, it is apparent that the relative error between the experimental and numerical ultimate displacement is smaller than 25%, for all specimens. Black dots are used to individuate the TUs depicted in Fig. 10 (i.e., LAP-P4, LAP-P16 and LAP-P5) and to demonstrate that the good model performance was not restricted to those cases. A remark is due to the fact that the database used for the current validation is the same employed to calibrate the deformation capacity of lap splices (Tarquini et al. 2019), and therefore acceptable matches were more likely regarding the ultimate displacement. However, to the authors' knowledge, no other experimental tests are available in the literature investigating the displacement capacity of lap splices. Moreover, the predictive equation proposed in Tarquini et al. (2019) was derived from the experimental data using a semi-empirical approach, i.e. including assumptions on the mechanical behaviour of the structural member (e.g., the contribution factor to the interface crack $\alpha = 0.5$). The performed validation hence strengthens the validity of such hypotheses, moreover confirming the dependability of the adopted mechanical approach.

Figure 11b, c show the relative average crack width error, for cracks located outside and within the lap-splice region, respectively. For each TU, the numerical and experimentally-measured crack widths of all cracks located in either of these two regions is computed and then averaged at each experimental peak tensile displacement. Again, the TUs used for validation in Fig. 10 are depicted with black lines; the points corresponding to the states A, B, and C, at which the crack widths were compared, are reported with the same marker notation. Results for all other TUs are represented in grey. For both cracks located outside and within the lapped zone, an error $\eta_w < 20\%$ (approximately) can be observed for all TUs and displacement levels. Exception is made for cracks along the lap-splice zone and low imposed displacements ($\Delta_{tot} < 3$ mm), where the error can arrive to 40%. This deviation can be partly attributed to the fact that experimental cracks, at such small tensile demands, may still evolve along the member (i.e. new cracks can open at different locations) while the points in which they are evaluated are fixed.

Finally, the relative contribution of the three model elements to the total ultimate displacement (at tensile failure) was computed. The results are plotted in Fig. 12, which shows that the different contributions do not vary significantly for the considered specimens. It represents approximately 20%, 60% and 20% for the anchorage, tension chord and lap splice elements respectively. It is also noted that the contribution from the anchorage region is fairly constant, which is expected since it does not depend on the lap splice length, transverse reinforcement or loading history.

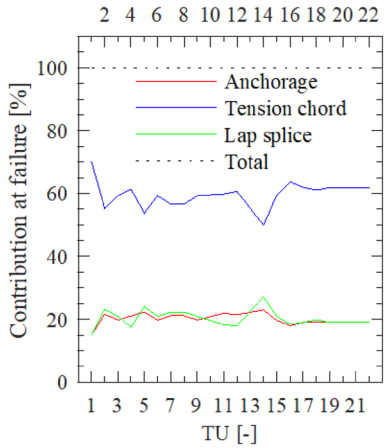

Fig. 12 Relative contribution of the three model elements to the total ultimate displacement (at tensile failure), as predicted by the model for all the test units.

5 Conclusions

Reinforced concrete walls often have lap splices above the foundation level, where the expected seismic demand is maximum. A proper detailing of lap splices is of fundamental importance for the cyclic response of the structural member as it can result in a significant reduction of its strength and deformation capacity. Boundary elements represent the most strained region of the RC wall, and therefore the one where lap splice failure is triggered.

In this paper, a mechanical model for the simulation of RC wall boundary elements with lap splices is presented. It is an extension of the tension chord model for continuous reinforcement. The model comprises three different types of elements connected in series: an anchorage element accounting for the strain penetration of the reinforcement into the foundation, a lap-splice element describing the deformation occurring within the spliced region and a basic tension chord element modelling the response outside the lapped zone. The lap-splice element is a novel contribution of the authors. It assumes that the force is transferred from the anchored to the free end (unloaded) rebar through concrete bond. It is further hypothesized that in the lap splice region the concrete transfers stresses from one rebar to the other but does not contribute significantly to the stiffness of the lap splice element (i.e. the tension stiffening effect is neglected). The model is highly versatile and allows any combination and number of the above-mentioned elements, the solution of which requires an iterative method. A new stable solution procedure is therefore proposed to solve the global nonlinear problem. The average lap splice strain at failure suggested by Tarquini et al. (2019) is herein used to determine the ultimate displacement of boundary elements with lap splices.

Finally, the model was validated against a set of 24 tests on RC wall boundary elements with both continuous and spliced longitudinal reinforcement. Different lap-splice lengths and confining reinforcement were also considered. Comparisons were made in terms of force–displacement response, crack width and strain distribution along the pair of spliced rebars. In all cases, and despite the fact that cyclic steel strength degradation and cyclic bond strength degradation are not accounted for in the model, a good match is found between numerical and experimental results; relative errors regarding the ultimate displacement and crack widths are on average below 20%.

List of Symbols

A_c: concrete area; A_s: longitudinal reinforcement area; A_t: total sectional area; E_c: concrete elastic stiffness; E_s: steel elastic stiffness; E_{sh}: steel plastic stiffness; EA/L: axial stiffness of the uncracked tension chord; f_{ct}: concrete tensile strength; f'_c: concrete compressive strength; f_y: steel yield strength; f_u: steel ultimate strength; h: test units height; L_0: total length of the RC wall boundary element (or of the tension chord); l_0: straight length of the anchored rebar; l_{ac}: length required to develop the steel strain at crack (ε_{ac}); $l_{ac,p}$: length required to develop the plastic portion of the steel strain at crack ($\varepsilon_{ac} - \varepsilon_y$); l_{anc}: anchorage length; l_b: development length required to pass from a pre-crack to a post-crack steel stress state; l_p: length required to develop the total rebar plastic strain ($\varepsilon_{ult} - \varepsilon_y$); l_s: lap splice length; l_y: development length required to achieve rebar yielding; $l_{y,eqF}$: distance between the yield point and the first point in which ε_{eqF} is reached; l_{ult}: development length required to achieve rebar rupture; N: imposed axial force; N_c: concrete force; N_{cs}: force required to attain crack stabilization; $N_{c,max}$: maximum force carried by the concrete (at *srm*/2) with reinforcement remaining elastic; $N_{c,max,p}$: maximum force carried by the concrete (at *srm*/2) with reinforcement that has yielded; N_s: steel force; N_{fc}: force required to attain first cracking; $N_{fc,lap}$: force required to attain first cracking within the lap splice region; srm: crack spacing; u_s: steel displacement; u_c: concrete displacement; w: crack width; δ: relative steel–concrete slip; Δ: imposed axial displacement; Δ_{anc}: slip of the anchored rebar at the interface; Δ_{comput}: total displacement of the boundary element computed internally (integral of ε_s); Δ_{ls}: total displacement of a lap splice element; Δ_{TC}: total displacement of a basic tension chord element; Δ_{tot}: total imposed displacement to the RC wall boundary element; ε_{ac}: steel strain at crack location; ε_c: concrete strain; ε_{cs}: minimum steel strain required to have crack stabilization; $\varepsilon_{c,srm/2}$: concrete strain at midway between two cracks (*srm*/2); $\varepsilon_{c,y}$: steel strain at the point corresponding to steel yielding ($\varepsilon_s = \varepsilon_y$); ε_{eqF}: steel strain at the point where steel and concrete stress are equal within the lap splice zone; ε_p: steel plastic strain ($\varepsilon_p = \varepsilon_s - \varepsilon_y$); ε_s: steel strain; $\varepsilon_{srm/2}$: steel strain at midway between two cracks (*srm*/2); ε_y: steel yield strain; ε_{ult}: ultimate steel strain; ϕ_l: longitudinal rebar diameter; η: relative error between numerical and experimental quantities; $\eta_{\Delta u}$: relative error on the ultimate displacement of the RC wall boundary element; $\eta_{w,out}$: relative error on the average crack width outside the lap spice region; $\eta_{w,lap}$: relative error on the average crack width within the lap spice region; ρ_l: longitudinal reinforcement ratio; ρ_t: transverse reinforcement ratio; σ_c: concrete stress; $\sigma_{c,max,p}$: maximum concrete stress between cracks (at *srm*/2) when the steel is in a post-yield state; σ_s: steel stress; $\sigma_{s,B}$: concrete stress before crack; $\sigma_{s,C}$: concrete stress after crack; τ_b: bond stress; τ_{b0}: elastic bond stress: the reinforcing steel is elastic ($\sigma_s < f_y$); τ_{b1}: plastic bond stress: the reinforcing steel has yielded ($\sigma_s > f_y$); v_{num}: generic numerical quantity; v_{exp}: generic experimental quantity.

Acknowledgements

The authors would like to thank Dr. Michele Godio for his precious help with the design of some figures.

Authors' contributions
DT developed the model and conducted the analysis under the supervision of JPA and KB.

Funding
The financial support by the Swiss Federal Roads Office (FEDRO) to the project number AGB 2015/002, under which the present study is carried out, is acknowledged.

Availability of data and materials
The files for producing the simulation results and for plotting Figs. 9, 10 and 11 are provided in the following public repository: https://zenodo.org/record/3353639#.XT3MJJMzZbU.

Competing interests
The authors declare that they have no competing interests.

Author details
[1] Earthquake Engineering and Structural Dynamics Laboratory (EESD), School of Architecture, Civil and Environmental Engineering (ENAC), École Polytechnique Fédérale de Lausanne (EPFL), EPFL ENAC IIC EESD, GC B2 495, Station 18, 1015 Lausanne, Switzerland. [2] Institute of Mechanics, Materials and Civil Engineering, UCLouvain, Place du Levant 1 L5.05.01, 1348 Louvain-la-Neuve, Belgium.

Received: 13 August 2019 Accepted: 26 November 2019
Published online: 24 January 2020

References

Almeida, J. P., Prodan, O., Tarquini, D., & Beyer, K. (2017). Influence of lap-splices on the cyclic inelastic response of reinforced concrete walls I: Database assembly, recent experimental data, and findings for model development. *Journal of Structural Engineering, 143,* 04017156.

Alvarez. M., (1998). *Einfluss des Verbundverhaltens auf das Verformungsvermögen von Stahlbeton*. Tech Rep, Inst Struct Eng Swiss Fed Inst Technol Zurich, Switzerland **(in German)**.

Canbay, E., & Frosch, R. J. (2005). Bond strength of lap-spliced bars. *ACI Structural Journal, 102,* 605–614.

CEB. (1978). *Model Code for Concrete Structures*. Paris: Comité Euro International du Béton.

EN 1992-Part 1-1. (2004). Eurocode 2: Design of concrete structures Part 1-1: General rules and rules for buildings.

Feng, D. C., & Xu, J. (2018). An efficient fiber beam-column element considering flexure–shear interaction and anchorage bond–slip effect for cyclic analysis of RC structures. *Bulletin of Earthquake Engineering*. https://doi.org/10.1007/s10518-018-0392-y.

FIB (2013) Model Code for Concrete Structures 2010. 434.

FIP-CEB. (1990). *Model Code 1990*. Lausanne: Fédération Internationale du Béton.

Kaufmann, W., (1998), *Strength and deformations of structural concrete subjected to in-plane shear and normal forces*. Tech. Report, Inst. Struct. Eng. Swiss Fed. Inst. Technol. Zurich, Switzerland.

Kaufmann, W., & Marti, P. (1998). Structural concrete: Cracked membrane model. *Journal of Structural Engineering, 124,* 1467–1475.

Marti, P., Alvarez, M., Kaufmann, W., & Sigrist, V. (1998). Tension Chord Model for Structural Concrete. *Structural Engineering International*. https://doi.org/10.2749/101686698780488875.

Muttoni, A., Fernandez, M. R., (2010). Structures en béton. Course notes, École Polytech. fédérale Lausanne, Switzerland.

Orangun, C. O., Jirsa, J. O., & Breen, J. E. (1977). A reevaluation of test data on development length and splices. *ACI Journal, 74,* 114–122.

Priestley, M. J. N., Calvi, G. M., & Kowalsky, M. J. (2007). *Displacement-based seismic design of structures*. Pavia: IUSS Press.

Priestley, M. J. N., Seible, F., & Calvi, G. M. (1996). *Seismic Design and Retrofit of Bridges*. New York: Wiley.

Sezen, H., & Setzler, E. J. (2008). Reinforcement Slip in reinforced concrete columns. *ACI Structural Journal, 105,* 280–289.

Sigrist, V. (1995). *Zum Verformungsvermögen von Stahlbetonträgern*. Tech. Report, Inst. Struct. Eng. Swiss Fed. Inst. Technol. Zurich, Switzerland. 210 **(in German)**.

Sigrist, V., Marti, P. (1994). Ductility of structural concrete: A contribution. In: *Proceedings Workshop Development of EN 1992 in Relation to New Research Results and to the CEB-FIP Model Code 1990* (pp. 211–223), Czech Technical University, Prague, Czech Republic.

Sousa, R., Almeida, J. P., Correia, A. A., & Pinho, R. (2018). Shake table blind prediction tests: Contributions for improved fiber-based frame modelling. *Journal of Earthquake Engineering*. https://doi.org/10.1080/13632469.2018.1466743.

Tarquini, D., Almeida, J. P., & Beyer, K. (2017). Influence of lap-splices on the cyclic inelastic response of reinforced concrete walls. II: Shell element simulation and equivalent uniaxial model. *Journal of Structural Engineering, 143,* 04017157.

Tarquini, D., Almeida, J. P., & Beyer, K. (2018). Uniaxial cyclic tests on reinforced concrete members with lap splices. *Earthq Spectra*. https://doi.org/10.1193/041418EQS091DP.

Tarquini, D., Almeida, J. P., & Beyer, K. (2019). Experimental investigation on the deformation capacity of lap splices under cyclic loading. *Bulletin of Earthquake Engineering, 17,* 6645–6670.

Tastani, S. P., Brokalaki, E., Pantazopoulou, S. J., & Asce, M. (2015). State of bond along lap splices. *Journal of Structural Engineering, 141,* 1–14. https://doi.org/10.1061/(ASCE)ST.1943-541X.0001243.

Zhao, J., & Sritharan, S. (2007). Modeling of strain penetration effects in fiber-based analysis of reinforced concrete structures. *ACI Structural Journal, 104,* 133–141.

Zuo, J., & Darwin, D. (2000). Splice strength of conventional and high relative rib area bars in normal and high-strength concrete. *ACI Structural Journal, 97,* 630–641.

Publisher's Note

Springer Nature remains neutral with regard to jurisdictional claims in published maps and institutional affiliations.

Submit your manuscript to a SpringerOpen journal and benefit from:

- ► Convenient online submission
- ► Rigorous peer review
- ► Open access: articles freely available online
- ► High visibility within the field
- ► Retaining the copyright to your article

Submit your next manuscript at ► springeropen.com